energies

MDPI

Article

Evaluation of Slag Foaming Behavior Using Renewable Carbon Sources in Electric Arc Furnace-Based Steel Production

Lina Kieush [1,*], Johannes Schenk [1], Andrii Koveria [2], Andrii Hrubiak [3], Horst Hopfinger [4] and Heng Zheng [1]

[1] Chair of Ferrous Metallurgy, Montanuniversitaet Leoben, 8700 Leoben, Austria
[2] Department of Chemistry, Dnipro University of Technology, 49005 Dnipro, Ukraine
[3] G.V. Kurdyumov Institute for Metal Physics of the National Academy of Sciences of Ukraine, 02000 Kyiv, Ukraine
[4] Chair of Ceramics, Montanuniversitaet Leoben, 8700 Leoben, Austria
* Correspondence: lina.kieush@unileoben.ac.at

Abstract: The influence of different carbon sources, including anthracite, calcined petroleum coke, three samples of high-temperature coke, biochar, and a mixture of 50 wt.% biochar and 50 wt.% coke, on slag foaming behavior was studied. The slag's composition was set to FeO-CaO-Al_2O_3-MgO-SiO_2, and the temperature for slag foaming was 1600 °C. The effect of the carbon sources was evaluated using foaming characteristics (foam height, foam volume, relative foaming height, and gas fraction), X-ray diffraction (XRD), chemical analysis of the slag foams, Mossbauer spectroscopy, observation by scanning electron microscope (SEM), and energy-dispersive spectroscopy (EDS) mapping. Different foaming phenomena were found among conventional sources, biochar as a single source, and the mixture of coke and biochar. Biochar showed the most inferior foaming characteristics compared to the other studied carbon sources. Nevertheless, the slag foaming process was improved and showed slag foaming characteristics similar to results obtained using conventional carbon sources when the mixture of 50 wt.% coke and 50 wt.% biochar was used. The XRD analysis revealed a difference between the top and bottom of the slag foams. In almost all cases, a maghemite crystalline phase was detected at the top of the slag foams, indicating oxidation; metallic iron was found at the bottom. Furthermore, a difference in the slag foam (mixture of coke and biochar) was found in the presence of such crystalline phases as magnesium iron oxide (Fe_2MgO_4) and magnetite ($Mg_{0.4}Fe_{2.96}O_4$). Notwithstanding the carbon source applied, a layer between the foam slag and the crucible wall was found in many samples. Based on the SEM/EDS and XRD results, it was assumed this layer consists of gehlenite ($Ca_2(Al(AlSi)O_7$) and two spinels: magnesium aluminate ($MgAl_2O_4$) and magnesium iron oxide (Fe_2MgO_4).

Keywords: electric arc furnace; slag foaming; carbon sources; biochar; steelmaking

Citation: Kieush, L.; Schenk, J.; Koveria, A.; Hrubiak, A.; Hopfinger, H.; Zheng, H. Evaluation of Slag Foaming Behavior Using Renewable Carbon Sources in Electric Arc Furnace-Based Steel Production. *Energies* **2023**, *16*, 4673. https://doi.org/10.3390/en16124673

Academic Editors: Marcin Sajdak, Roksana Muzyka and Grzegorz Gałko

Received: 28 May 2023
Revised: 8 June 2023
Accepted: 10 June 2023
Published: 12 June 2023

1. Introduction

The practice of foaming slag is widely used in electric arc furnace (EAF) operations to achieve many benefits, including saving electricity, protecting the furnace lining, and reducing electrode consumption [1–8]. Slag foaming is also interesting for basic oxygen steelmaking [9–11] and ladle processing [12]. The foaming formation of the slag is influenced by the gas phase, which is determined by the amount of CO/CO_2 created, as well as by the slag phase, which determines the foamability [13–15].

In the interaction between carbon and slag in EAF, the phenomenon of slag foaming occurs, which involves the trapping of gas bubbles in the slag layer when a carbon-bearing source interacts with iron oxide in the slag. This gas foams the slag, increasing its volume depending on parameters such as the type of carbon source used, the FeO content of the slag, the slag's basicity, temperature, etc. Reduction reactions and slag foaming in EAF operations depend not only on the physicochemical properties of the slag [16] but also on the carbon source. Some technological limits regarding the use of

carbon sources in EAF include low volatile matters (VM) of 2–7%, low moisture of 1–7%, a particle size of 0.5–5 mm, and low alkalis [17]. An important factor is the reactivity of the carbon source, which affects the chemical reactions that create the gas phase. On the other hand, the ash composition of the carbon-bearing source affects the slag phase and can change factors such as slag viscosity and surface tension. Changes in basicity and P_2O_5 content could be possible.

Several authors [12,18] have experimentally evaluated the phenomenon of slag foaming using conventional carbon sources. The effect of carbon-bearing particles (coke or coal) on the size and shape of slag foam has been studied. It has been established that carbon particles have a defoaming effect due to their non-wettability [19–22]. Therefore, the optimal amount of the FeO and C in the system is required, since excess carbon, instead of promoting gas-generating reactions, can reduce foam stability. Additionally, studies on the influence of the type of carbon-bearing source showed that the reduction in FeO and, therefore, the reaction kinetics depend on the type of carbon source.

Corbari et al. [23] used five different types of carbonaceous material—graphite, bituminous coal, bituminous char, anthracite coal, and anthracite char—to study the foaming process. The composition of the slag included CaO, SiO_2, MgO, and FeO within the range of 15 to 45 wt.%. This investigation showed that additional gas was released in the form of VM when using coal. However, VM is less effective than CO released from the slag foaming reaction. This is because the gas bubbles produced by the reaction were smaller, resulting in a more stable foam.

Ji et al. [24] used industrial slags of CaO–SiO_2–MgO–Al_2O_3–FeO with 30–40 wt.% FeO. As a carbon source, anthracite was used. According to the tests, the maximum carbon addition speed was 10 g of carbon per minute per kilo of slag. If the carbon amount was higher than this value, an excess of these particles was observed in the system. Additionally, it was noticed that the quantity of unreacted carbon particles acted to destabilize the formed foam.

Zhang and Fruehan [20] evaluated the influence of carbonaceous particles, namely, coke or coal char (with various sizes), in the foaming index when using forced argon injection at 1500 °C. The slag composition in this study used CaO–SiO_2–CaF_2–Al_2O_3. In some cases, the foam formation was suppressed due to the covering of the slag surface with carbon. Moreover, it was concluded that the bubbles generated by the reaction of FeO-C, which were small (from 1 to 3 mm), gave a more stable foam than bigger bubbles, consistent with the conclusions in the paper [23].

Aiming to reduce dependence on fossil fuels and decrease the contribution to greenhouse gas (GHG) emissions in EAF steelmaking, various authors have evaluated the slag foaming phenomenon and the impact on foaming behavior when using non-conventional carbon sources. Generally, studies focus on biochar use [25–27] and a mixture of biochar and coke [28]. Further, there are studies on waste plastics and rubber applications [29–31].

Maroufi et al. [32] studied the chemical interaction of EAF slag (Fe_2O_3-SiO_2-Al_2O_3-CaO-MgO-MnO) with three different carbon sources: coke, rubber-derived carbon, and a mixture of coke and rubber-derived carbon at atmospheric pressure at 1550 °C. The high reactivity of rubber-derived carbon led to a rapid interaction with molten slag. However, a low reduction rate of iron oxide from the slag was observed when using rubber-derived carbon, which was explained by the initial weak contact between rubber-derived carbon and molten slag. This led to the conclusion that the interaction between the carbonaceous material and the slag plays a significant role in the iron oxide reduction from slag.

Yunos et al. [33] investigated the possibility of using biomass in the EAF, namely, palm shell char, to partially replace coke in a laboratory-scale reactor at 1550 °C using the sessile-drop approach in an argon atmosphere. The slag composition in this study was set as Fe_2O_3–CaO–Al_2O_3–MgO–SiO_2–MnO. The test results showed an improved interaction with EAF slag compared to conventional coke.

Fidalgo et al. [34] studied two biochars obtained from agricultural residues, grape seed, and pumpkin seed chars for EAF steelmaking. Hard coal and three types of anthracite

were also used to compare the results. The authors found that biochar could replace coal. Furthermore, it was noted that the highly volatile matters of biochar are an adequate stimulation for slag foaming.

Huang et al. [35] studied the interaction between synthetic slag with a composition of CaO–Fe_2O_3–Al_2O_3–MgO–SiO_2–MnO and carbon materials obtained from various sources, including biochar, graphite, coke, and coal obtained from tire pyrolysis at a temperature of 1600 °C. Various interfacial phenomena were found between the slag and the investigated carbonaceous materials. The interaction between the biochar and slag was weak compared to other carbonaceous materials. The smooth surface of the biochar was claimed to decrease slag foaming.

The project entitled "Sustainable EAF steel production (GreenEAF)" [13] was devoted to studying the partial or full substitution of coal and natural gas by charcoal or syngas produced by the pyrolysis of biomass in EAF steel production. One of the interesting findings was that the tested charcoal gave only poor foaming results. The most obvious difference is the variable wettability, which, in the case of charcoal, prevents the reaction between the FeO in the slag and the carbon and, therefore, the formation of CO bubbles. The content of the VM in the carbon sources in these tests did not influence the foaming of the slag.

Echterhof [36] presented a review of the research related to the laboratory- and industrial-scale investigation of alternative carbon sources to replace the conventional carbon sources in EAF. The author also revealed that there is still much potential and a necessity for further research in this area.

This paper aims to analyze and compare slag foaming behavior using partially or entirely renewable carbon sources; to establish the effect of various carbon sources on foaming characteristics at 1600 °C as well as the composition of the slag foams; and to show the possibility of using renewable carbon sources for EAF applications to replace conventional carbon sources either partially or entirely.

2. Materials and Methods

For slag foaming tests, slag with the composition shown in Table 1 was prepared from a homogeneous mixture of FeO, MgO (≥98%), CaO (≥96%), SiO_2 (≥99%), and Al_2O_3 (≥99%) powders. The slag density and surface tension were calculated according to [37], and the foaming index was calculated according to [38]. Slag viscosity was determined via FactSage v.8.2.

Table 1. Target slag composition for slag foaming tests.

FeO, wt.%	SiO_2, wt.%	Al_2O_3, wt.%	MgO, wt.%	CaO, wt.%	B2	B3	ρ g/cm^3	η Pa·s	γ N·m^{-1}	Σ s
28.0	19.4	9.1	11.9	31.6	1.6	1.1	3.44	0.0382	0.568	0.863

Basicity (B2), CaO/SiO_2; basicity (B3), CaO/SiO_2 + Al_2O_3; ρ, density; η, viscosity; γ, surface tension; Σ, foaming index or average traveling time of the gas in the generated foam.

An alumina crucible (height 99 mm, inner diameter 63 mm, and wall thickness 4 mm) was filled with ultra-low carbon (ULC) steel of approximately 5 g (Table 2) and 100 g of slag.

Table 2. Chemical composition of ULC steel.

Elements	wt.%
C	0.007
Fe	99.6

The filled alumina crucible was placed in a graphite crucible (height 202 mm, inner diameter 70.3 mm, and wall thickness 20 mm) and flushed with nitrogen at a rate of 1000 L/h during each test.

The carbon content was calculated stoichiometrically for the required reduction according to the equation FeO (slag) + C = Fe (1) + CO [39,40]. The following carbon sources (Table 3) were used in this study: anthracite (Anth), calcined petroleum coke (CPC), high-temperature metallurgical coke samples (Coke1, Coke2, and Coke3), and wood biochar pellets (Bch), which were used with stable grain size from 0.5–1.0 mm to avoid the influence of particles on the size and behavior of slag foam.

Table 3. Characteristics of carbon sources used for slag foaming.

Characteristics	Anth	CPC	Coke1	Coke2	Coke3	Bch
Proximate analysis (wt.%)						
M	5.91	0.75	1.04	0.82	0.78	2.67
VM (db)	3.69	0.44	1.42	0.95	0.74	39.28
VM (daf)	4.12	0.45	1.57	1.03	0.80	41.04
Ash (db)	10.50	0.90	10.88	11.03	11.09	4.29
Elemental analysis (wt.%)						
S (db)	0.48	0.62	0.77	0.56	0.59	n.d.
C (db)	82.58	97.01	86.25	86.50	86.55	72.74
H (db)	2.19	0.26	0.29	0.23	0.21	4.62
N (db)	0.97	0.94	1.21	1.15	1.11	0.24
* Others, mainly O (db)	3.28	0.27	0.6	0.53	0.45	18.11
C_{fix} (db)	85.81	98.66	87.70	88.02	88.17	56.43
Characteristics of microstructural parameter (nm)						
L_c	2.08	1.58	1.86	1.56	1.32	0.69

M, moisture; C, carbon; H, hydrogen; N, nitrogen; S, sulfur; db, dry basis; daf, dry ash-free basis; VM(daf) = VM(db)·100/(100 − ash yield (db,%)); C_{fix}, wt.% = 100 − (wt.% VM (db) − wt.% Ash (db)); * calculated by difference; n.d., not detected; L_c, crystallite height.

All foaming tests were carried out using an induction high-temperature furnace MU-900 (Indutherm Erwärmungsanlagen GmbH) (Figure 1).

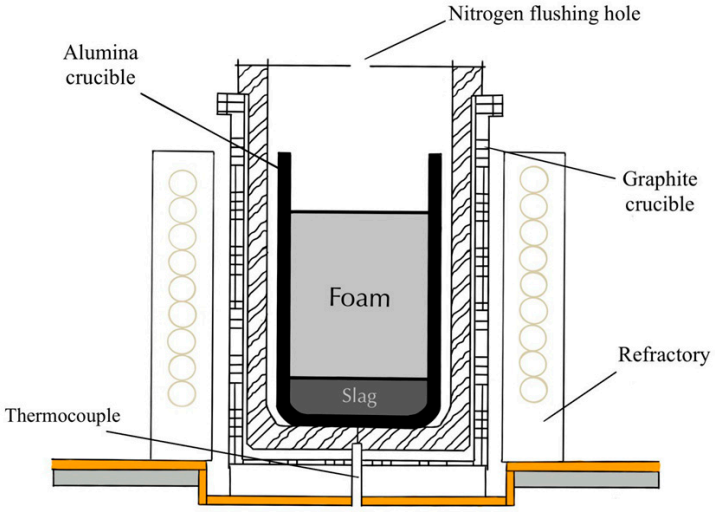

Figure 1. Experimental setup for the slag foaming tests.

When the temperature reached 1600 °C, a holding time of 15 min took place. The height of the molten slag was measured by dipping a molybdenum stick into the molten slag and then measuring the trace that remained on the stick with a ruler. Afterward, the carbon source was added, and the molten slag was mixed with a molybdenum stick, intensifying the carbon–slag reaction until the foam was stable. Due to the difference in density between the slag and the carbon, the carbon particles covered the surface of the slag and suppressed the foaming process. Stirring contributed to the penetration of carbon sources into the molten slag.

The standard time for foaming, regardless of the carbon source, was 6 min, which proved experimentally adequate for the carbon source to undergo a reaction. After the end of the test, the alumina crucible was quenched with liquid nitrogen to solidify the foam structure and prevent the foam from breaking. Each test was repeated four times for each carbon source.

A further alumina crucible with solidified foam was filled with the hardeners PUR 145 and SG 141/10 to prepare samples to be cut for examination. The samples were cut both horizontally and vertically and examined by microscopes.

Based on the foaming height, the volume of slag before (V_{slag}) and after foaming (V_{foam}) was calculated using Equations (1) and (2):

$$V_{slag} = \frac{d^2 \cdot \pi}{4} \cdot h_{slag}, \quad (1)$$

$$V_{foam} = \frac{d^2 \cdot \pi}{4} \cdot h_{foam}, \quad (2)$$

where d is the inner diameter of the crucible, cm; h_{slag} is slag height before foaming, cm; h_{foam} is slag height after foaming, cm.

Additionally, the slag weight (Table 1), the inner diameter of the alumina crucible, the slag density (Table 1), and Equation (1) were used to calculate the initial slag height without foaming.

The relative foaming height ($\frac{\Delta h}{h_0}$) was calculated by Equation (3):

$$\frac{\Delta h}{h_0} = \frac{h_{foam} - h_{slag}}{h_{slag}}, \quad (3)$$

The foaming height was estimated after the experiments, and the volumetric gas fraction contained in the foam (X_{gas}) was also calculated using Equation (4), according to [41,42].

$$X_{gas} = \frac{h_{foam} - h_{slag}}{h_{foam}}, \quad (4)$$

where h_{foam} is the slag height after foaming, cm; h_{slag} is the slag height before foaming, cm.

Additionally, the relative amount (ΔFeO) was calculated using Equation (5):

$$\Delta FeO = \frac{FeO_{slag} - FeO_{foam}}{FeO_{slag}} \times 100\%, \quad (5)$$

where FeO_{slag} is the amount of FeO in the initial slag composition, wt.%; FeO_{foam} is the amount of FeO in the slag composition after foaming, wt.%.

The chemical composition of the solidifying foam structure at the top and bottom of the crucible was determined by manganometrical titration according to Zimmermann-Reinhard (Fe_{tot} and Fe^{2+}), gravimetrical determination from lithium-tetraborate digestion (SiO_2), and inductive coupled plasma-optical emission spectroscopy from lithium tetraborate digestion (CaO, Al_2O_3, MgO).

X-ray diffraction (XRD) spectra of powdered slag foam samples were obtained using a Bruker AXS D8 advance diffractometer with a lynxeye detector and a Cu X-ray tube with Cu Kα radiation.

The magnetic microstructure of the samples and the state of their iron nuclei were studied using Mossbauer spectroscopy using the MS-1104Em spectrometer. The source of γ-quanta was the Co^{57} isotope in the chromium matrix. The natural width of the metal line α-Fe was 0.21 mm/s. The calibration of the isomeric shifts was carried out relative to α-Fe. Mossbauer spectra were interpreted using Univem MS analytical software.

Images of samples and mapping were obtained via a scanning electron microscope SEM FEI Quanta 200Mk2 equipped with an energy-dispersive (EDS) detector, back-scattered electron (BSE) detector, and a digital microscope Keyence VHX-E20.

3. Results and Discussion

Table 4 shows the calculated characteristics of the slag, namely, the height (h_{calc}) and volume (V_{calc}), which correspond to 0.93 cm and 29.1 cm^3.

Table 4. Calculated slag characteristics.

Calculated Slag Height h_{calc}, cm	Calculated Slag Volume V_{calc}, cm^3
0.93	29.1

Depending on the different carbon sources used, the foaming behavior of the slag was evaluated using the foaming characteristics shown in Table 5. It is noteworthy that with biochar, the height of the slag foam (SF) and the volume of the foam is lower compared with other carbon sources. Similar foaming behavior in the case of using biochar was noticed in [35] due to the low wettability of biochar by liquid slag, which prevents the reaction of carbon with FeO by the formation of a sufficient amount of CO bubbles [13]. Another reason is that due to the high reactivity of the biochar [43–45], FeO did not have time to react completely, and a smaller amount of CO was released, as evidenced by the value of the gas fraction (0.85). Among the carbon sources used, biochar is characterized by its low density, and therefore, when adding biochar particles, they were covered only on the surface of the slag foam. At the same time, stirring was difficult, because the biochar burned out on the slag foam surface very fast. As previously reported by [46], hydrogen in carbon sources can positively contribute to the FeO reduction reaction in the slag. However, based on the results presented in Table 5, when using biochar, which has the highest hydrogen value (4.62 wt.%), the lowest values in the height (6.5 cm) and volume of slag foam were obtained (201.9 cm^3).

It should be noted that when using anthracite with a hydrogen content of 2.19 wt.%, suitable slag foaming characteristics were obtained (8.7 cm and 272.1 cm^3 for foam height and foam volume, respectively). At the same time, the highest values were obtained when using coke2 (foam height of 8.9 cm and foam volume of 277.7 cm^3), as well as for coke1 (foam height of 8.3 cm and foam volume of 259.9 cm^3) and coke3 (foam height of 8.1 cm, and foam volume of 254.5 cm^3).

Using three samples of coke, anthracite, and calcined petroleum coke showed that the characteristics of the foams are similar.

Meanwhile, using 50 wt.% biochar in the mixture with coke 50 wt.% improved slag foaming characteristics (height, volume, relative foaming height, and gas fraction) compared to using biochar as a single carbon source for the foaming process. As noted during the tests, the improvement in these characteristics is due to the fact that 50 wt.% coke mitigated the drawbacks of using biochar and had a more significant effect on the foaming process than highly reactive biochar, particles of which burned very fast on the surface of the slag. Based on the results presented in Table 5, it can be concluded that the mixture of coke and biochar allows for obtaining foaming characteristics similar to using 100 wt.%

anthracite and at a level related to other coke samples. This can be explained by the fact that the change in physicochemical properties within the carbon source mixture, such as changes in surface area, density, and reactivity, exhibited a noticeable impact on the foaming mechanism, particularly when compared to individual carbon sources.

There is a statistically significant difference between the values of the height and the volume of slag foam samples as determined by one-way ANOVA (F value = 20.83, $p = 7.8 \cdot 10^{-8}$; and F value = 20.79, $p = 7.9 \cdot 10^{-8}$, respectively).

It is worth noting that the VM from the biochar (41.04 wt.%, daf) could also contribute to the foaming process, since the VM are released when the biochar is heated and could contribute to the foaming of the slag. However, the gas from the VM is less efficient than the gas from the chemical reaction of slag to foam, as previously shown in [12].

In the case of anthracite, this can be explained by the phenomenon of crushing coal particles in the process of releasing VM, which increased the surface area and, in turn, increased the rate of CO formation and, consequently, the height and volume of the slag foam. This phenomenon was also observed in [23]. Of note is that slag foam samples produced using anthracite as a carbon source show a vaster standard deviation for the height and volume characteristics of the slag foam compared to other carbon sources obtained by carbonization.

Notably, the slag is better wetted by a material with a similar chemical composition [35], and to achieve a good foaming process, it is required that carbon-bearing sources have relatively low ash content. However, biochar showed the most inferior foaming characteristics, although it is characterized by the lowest ash content (4.29 wt.%).

Typically, the gas fraction of slag foam is within the range of 0.80–0.95 [3]. The gas fractions vary between approximately 0.85–0.89, and the relative foaming heights between $\Delta h/h_0 = 5.8–8.4$. It has been observed that the lower the value of the gas fraction, the lower the relative foaming height (Figure 2).

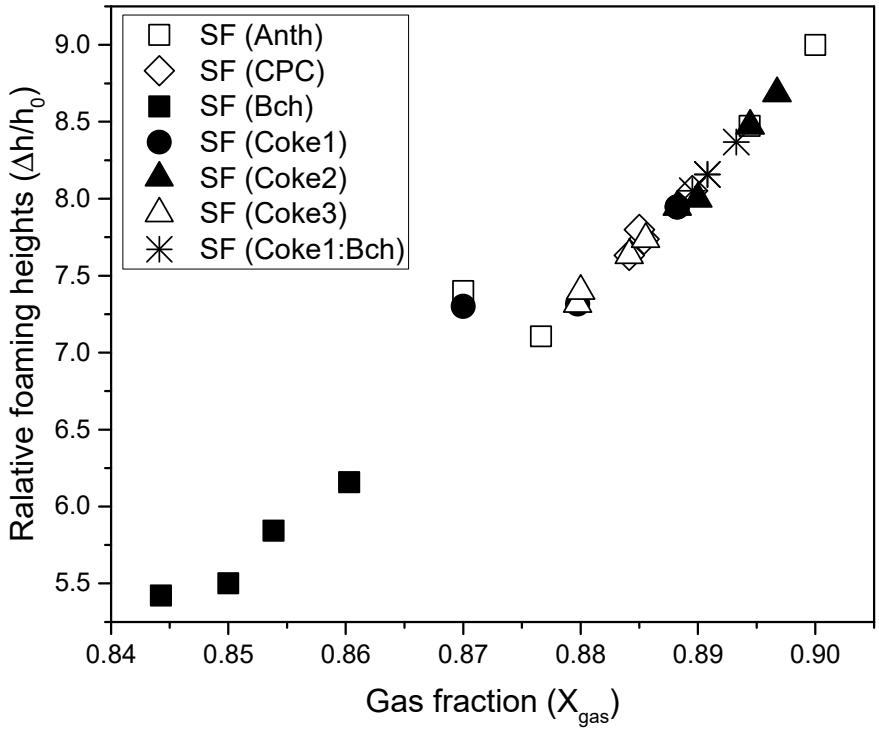

Figure 2. Relationship between gas fraction values and relative foaming heights, considering all values obtained after four tests.

Table 5. Summary results of slag foaming characteristics after four test sets.

Sample	Experimental Slag Height Mean h_{slag}, cm	std	Experimental Slag Volume Mean V_{slag}, cm^3	Std	Foam Height Mean h_{foam}, cm	std	Foam Volume Mean V_{foam}, cm^3	Std	Relative Foaming Height Mean $\Delta h/h_0$	Gas Fraction Mean X_{gas}
SF (Anth)	0.95	0.05	30	1.5	8.7	0.8	272.1	23.6	8.2	0.89
SF (CPC)					8.3	0.2	260.5	5.3	7.8	0.88
SF (Coke1)					8.3	0.3	259.9	9.2	7.7	0.89
SF (Coke2)					8.9	0.3	277.7	9.2	8.4	0.89
SF (Coke3)					8.1	0.2	254.5	5.8	7.6	0.88
SF (Bch)					6.5	0.3	201.9	9.0	5.8	0.85
SF (Coke1:Bch 50 wt.%:50 wt.%)					8.7	0.1	271.8	3.9	8.2	0.89

std, standard deviation.

Figure 3 shows the weight ratio of the carbon source to the slag and the effect on the foam height ratio. The amount of carbon material for tests was calculated stoichiometrically based on the amount of fixed carbon for each carbon source. Accordingly, the weight ratio of biochar to slag is the highest, and the foam height ratio is the lowest.

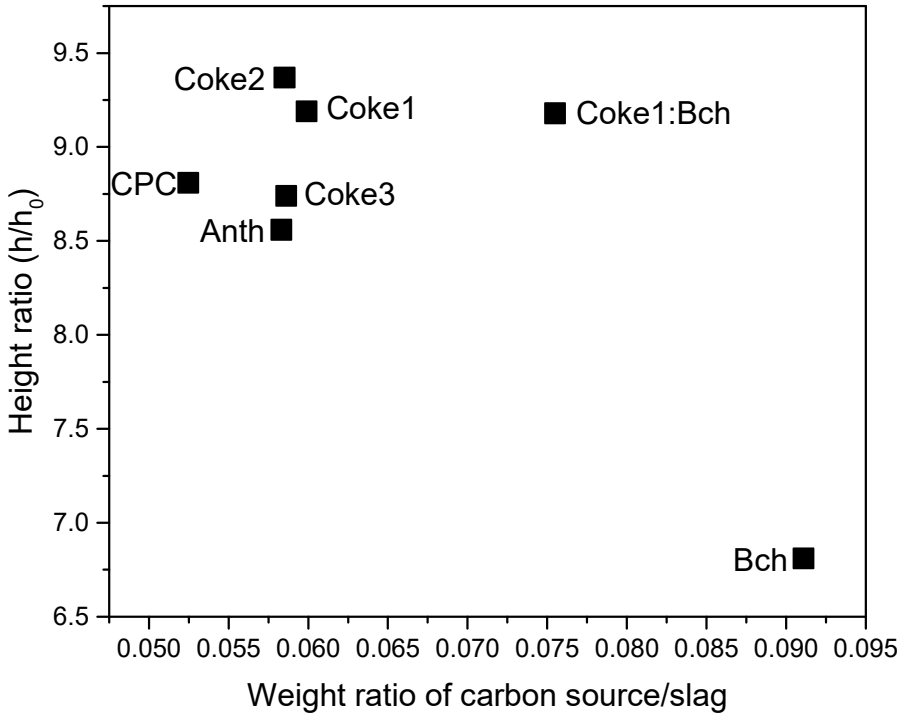

Figure 3. Weight ratio of carbon source/slag and ratio of slag heights.

However, the result of slag foaming changed with the partial use of biochar 50 wt.% with coke 50 wt.%, and the values became closer to the use of conventional carbon sources.

Selected examples of slag foams using different carbon sources are shown in Figure 4a–g. The results presented in Table 5 indicate that the VM and ash composition of carbon-bearing sources does not significantly contribute to slag foaming. Additionally, for VM, this can be explained by the large gas bubbles that formed, as shown in Figure 4a–g, which also complicated the process of creating stable foam.

Moreover, the results revealed the importance of the structural characteristics of the carbon sources used. A relationship was noticed between the XRD structural parameter crystallite height (L_c) of carbon sources and some slag foaming characteristics (Figure 5a). An increase in the structural ordering of the carbon material contributed to obtaining better slag foaming. Furthermore, Figure 5b shows the relationship between fixed carbon and slag foaming characteristics (slag foam height and slag foam volume), according to which the foaming process is better at higher values of fixed carbon in carbon sources, which confirms the conclusion that the higher fixed carbon, the better the slag foaming process [25].

Results of the ANOVA analysis showed the significance of the influence of fixed carbon content in carbon sources and the slag foaming characteristics of foam height and foam volume. Additionally, the influence of structural parameter crystallite height on foam height and foam volume was determined.

Figure 6a,b present the results of the XRD analysis of EAF slag foams obtained using different carbon sources. XRD analysis allowed for the identification of the following main crystalline phases at the top of the foams: gehlenite ($Ca_2(Al(AlSi)O_7$), wuestite (FeO), bredigite ($Ca_{1.7}Mg_{0.3}SiO_4$), merwinite ($Ca_3Mg(SiO_4)_2$), and maghemite (Fe_2O_3).

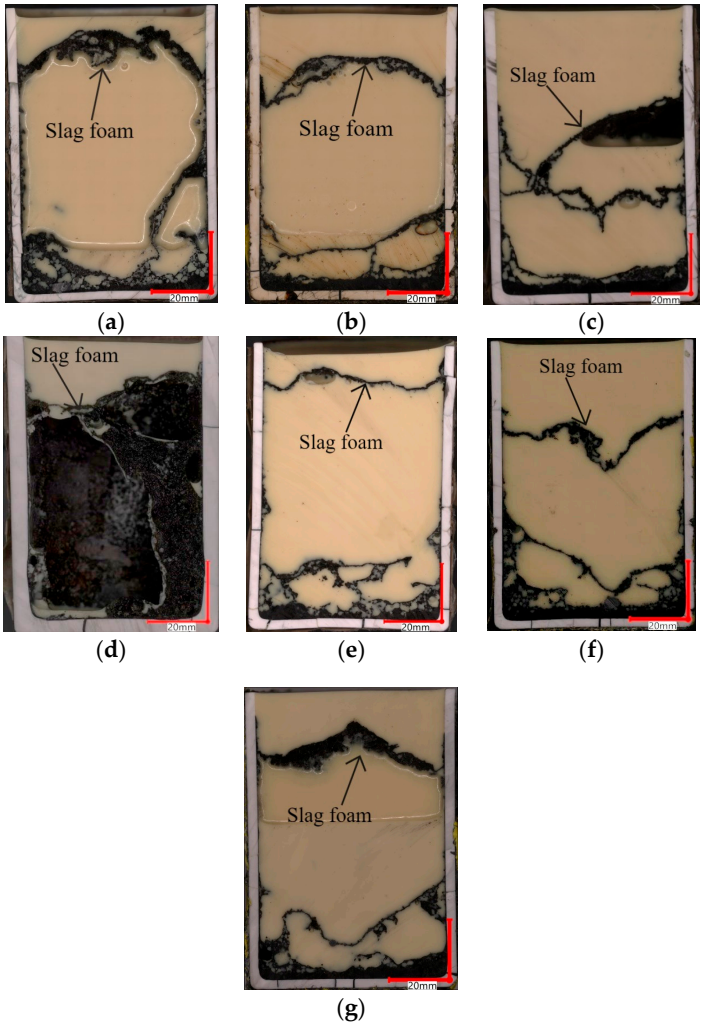

Figure 4. Examples of slag foams using different carbon materials: (**a**) slag foam obtained using anthracite; (**b**) calcined petroleum coke; (**c**) coke1; (**d**) biochar; (**e**) coke2; (**f**) coke3; and (**g**) 50 wt.% coke1: 50 wt.% biochar.

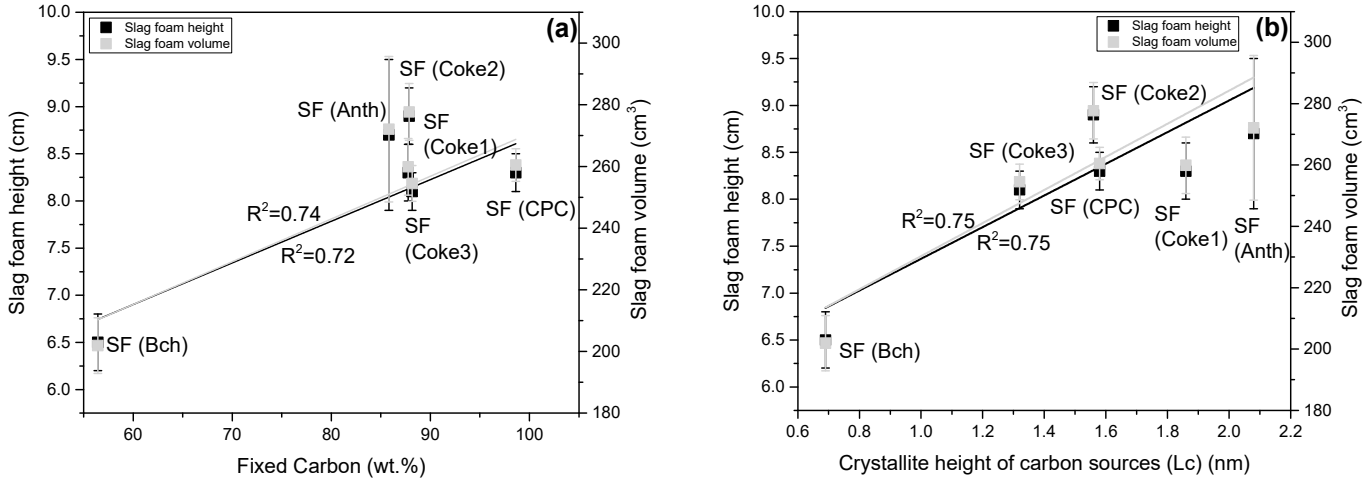

Figure 5. (**a**) Relationship between structural parameter crystallite height (L_c) for carbon source and slag foaming characteristics (foam height and foam volume); (**b**) relationship between amount of fixed carbon in carbon sources and slag foaming characteristics (foam height and foam volume).

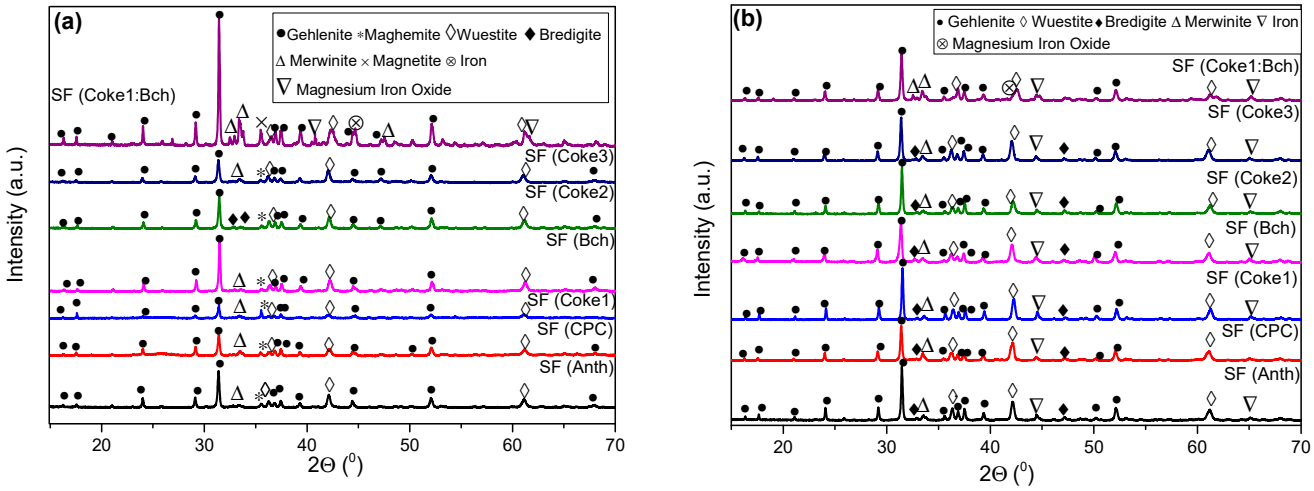

Figure 6. XRD patterns of slag foams obtained with different carbon sources: (**a**) at the top of the crucible; (**b**) and at the bottom of the crucible.

A small peak corresponding to the maghemite crystalline phase at the top of the slag foam can be explained as follows. Despite the fact that the crucible was flashed by nitrogen during the test, this did not contribute to a complete avoidance of oxidation. The maghemite crystalline phase was not detected for the lower part of the slag.

The slag foam at the bottom of the crucible indicated the following main crystalline phases: gehlenite, wuestite, merwinite, and metallic iron (Fe). Metallic iron was detected only in the samples from the bottom of the crucible. It should be noted that using non-conventional carbon sources did not significantly affect the crystalline phases compared to the presence of crystalline phases in slag foams obtained using conventional carbon sources.

In the case of slag foam, which was used as a carbon source, a mixture of coke1 and biochar XRD analysis confirmed the following crystalline phases at the top of the foams: gehlenite, wuestite, merwinite, and metallic iron (similar to other studied samples). The difference from the previous samples is the presence of such phases as magnesium iron oxide (Fe_2MgO_4) and magnetite ($Mg_{0.4}Fe_{2.96}O_4$). The slag foam at the bottom of the crucible contains gehlenite, wuestite, merwinite, magnesium iron oxide, and metallic iron. For this sample, no difference was observed between the crystalline phases for the top and bottom of the crucible.

The presence of magnetite in the top part of the slag foam, as in previous samples of slag foam where maghemite was found, is explained by the higher valence iron oxide, probably located in the slag foam region in contact with the air [47].

Due to the reduction in FeO in the slag during experiments, the slag foams' chemical composition was analyzed and is presented in Tables 6 and 7. The use of conventional or non-conventional carbon sources did not significantly affect the chemical composition of the slag selected at the top of the crucible after foaming. The range composition of the slag foams is 13.97–20.60 wt.% Fe_{tot}; 14.09–18.90 wt.% SiO_2; 29.72–33.03 wt.% CaO; 12.45–18.03 wt.% Al_2O_3; 5.51–9.80 wt.% MgO.

It should be noted that the high content of Al_2O_3 in the slag foam samples for both the top and bottom of the crucible can be explained by the presence of impurities from the alumina crucible.

Table 7 shows the chemical composition of the slag at the bottom of the crucible after foaming. The range composition of the slag foams is 17.69–34.10 wt.% Fe_{tot}; 12.13–17.68 wt.% SiO_2; 23.18–31.37 wt.% CaO; 14.16–17.00 wt.% Al_2O_3; 5.15–10.66 wt.% MgO.

Table 6. Chemical composition of the slag at the top of the crucible after foaming, wt.%.

Sample	Fe_{tot}	Fe^{2+}	SiO_2	CaO	Al_2O_3	MgO	B2
SF (Anth)	17.66	15.14	16.73	32.98	17.26	5.51	1.9
SF (CPC)	16.60	16.32	17.67	31.48	18.03	7.21	1.8
SF (Coke1)	16.71	16.37	16.88	30.79	16.95	7.13	1.8
SF (Coke2)	15.49	15.39	18.89	32.96	17.69	7.51	1.7
SF (Coke3)	19.21	18.99	17.05	29.72	17.55	6.90	1.7
SF (Bch)	13.97	11.57	18.90	33.03	17.49	6.88	1.7
SF (Coke1:Bch)	20.60	19.60	14.09	30.00	12.45	9.80	2.1

Table 7. Chemical composition of the slag at the bottom of the crucible after foaming, wt.%.

Sample	Fe_{tot}	Fe^{2+}	SiO_2	CaO	Al_2O_3	MgO	B2
SF (Anth)	23.72	23.67	15.77	28.89	15.10	6.97	1.8
SF (CPC)	18.92	16.06	15.69	30.90	15.96	6.73	1.9
SF (Coke1)	18.57	16.01	16.20	31.20	17.00	6.44	1.9
SF (Coke2)	17.69	17.14	17.68	31.37	16.99	7.39	1.8
SF (Coke3)	18.76	16.26	15.93	29.89	16.56	6.50	1.9
SF (Bch)	34.10	31.72	12.13	23.18	14.16	5.15	1.9
SF (Coke1:Bch)	21.12	20.00	12.36	28.07	14.64	10.66	2.3

The content of Si, Ca, and Mg oxides does not differ significantly between the samples from the top and bottom of the crucible and between different carbon sources. The reason for the decrease in the MgO content in all samples can be explained by the activity of MgO with some other slag components [48,49].

The decrease in the amount of Fe^{2+} after the foaming of the slag indicates a reduction reaction. Notably, high iron content was observed only for the slag foam SF (Bch) sample taken from the bottom of the crucible. As evidenced by XRD analysis (Figure 6b), metallic iron was detected at the bottom of each slag foam sample. Thus, the increase in iron content for SF (Bch) can be explained by the influence of oxidation of the slag foams from Fe to FeO during tests. When biochar was used, additional gas in the form of VM was released, contributing to oxidation and eventually decreasing foaming. This is confirmed by the slag foam height and volume results when using biochar that are given in Table 5.

Slag foaming characteristics were measured and evaluated in a comparison of changes in Fe (total) content in the slag after tests both for the top and bottom sides of crucibles, and the results are summarized and plotted in Figure 7a,b. Notably, when using biochar, the Fe (total) content is the lowest for the upper part of the crucibles, as are the slag foaming values. At the same time, the Fe (total) content is the highest in the lower part of the crucibles.

The relative amount of FeO is presented in Table 8. The decrease in FeO content in the slag foam samples both for the top and bottom of the crucible is irregular and indicates the presence of a reduction in FeO. Considering the results presented in Tables 5 and 8, it becomes evident that the incorporation of a coke1 and biochar mixture not only positively influenced the foaming process, but this also showed a more significant effect on the reduction in FeO compared to using individual carbon sources.

Figure 8a shows the SEM image of the interface between the foaming slag and the crucible. The EDS layered image (Figure 8b) shows that between the foamed slag and the crucible, there is a layer mainly composed of Mg, Al, Ca, Fe, and O. This phenomenon was observed for many samples under study, unrelated to the type of carbon source in the experiments.

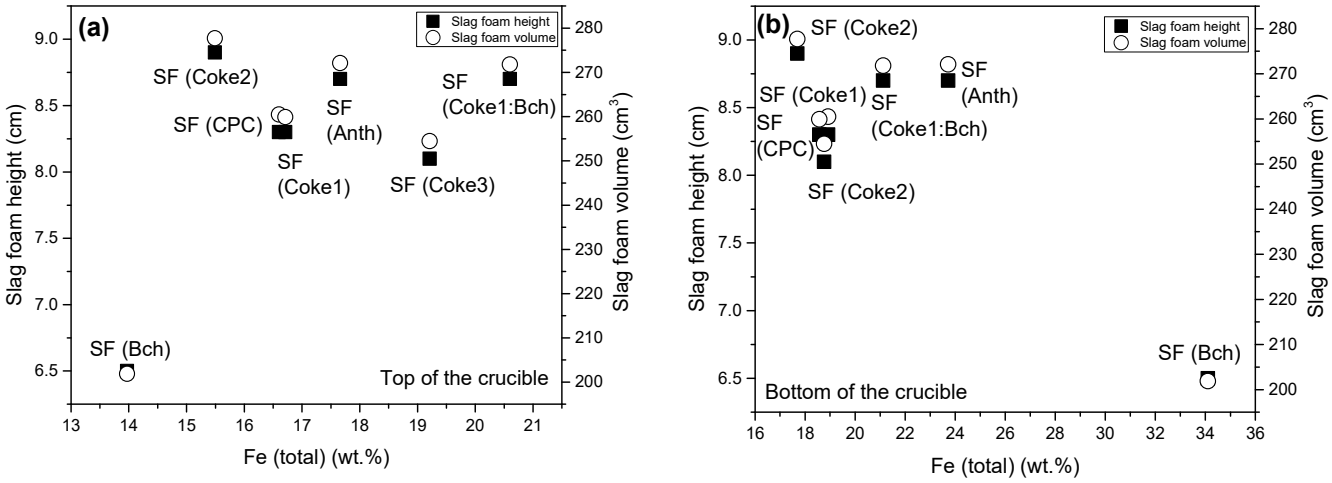

Figure 7. (**a**) Content of Fe (total) and slag foaming characteristics (height and volume) at the top of the crucibles; (**b**) content of Fe (total) and slag foaming characteristics (height and volume) at the bottom of the crucibles.

Table 8. Relative amount of FeO of the slag foam collected at the top and bottom of the crucible.

Sample	Relative amount ΔFeO_{top}, wt.%	Relative amount ΔFeO_{bottom}, wt.%
SF (Anth)	45.9	15.5
SF (CPC)	41.7	42.6
SF (Coke1)	41.5	42.8
SF (Coke2)	45.0	38.8
SF (Coke3)	32.2	41.9
SF (Bch)	58.7	n.a.
SF (Coke1:Bch)	30.0	28.6

n.a., not available.

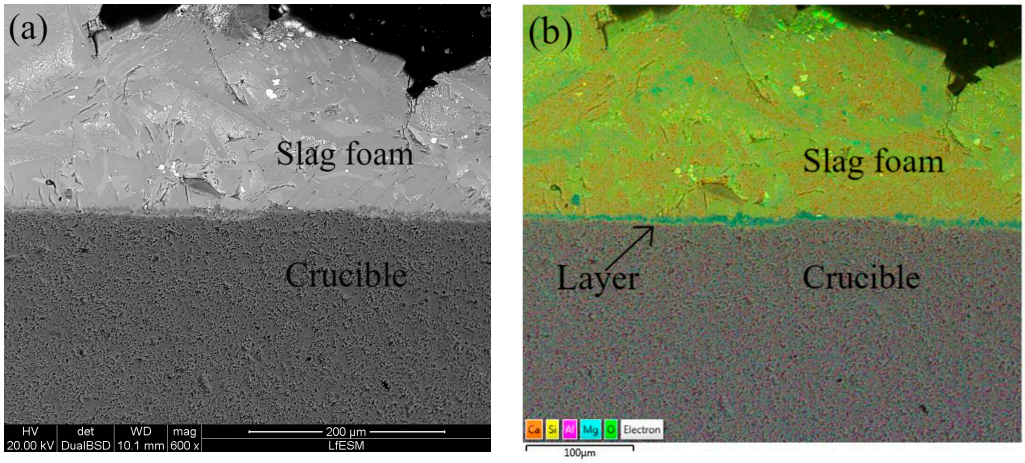

Figure 8. (**a**) SEM image of slag foam, layer between slag foam and wall of crucible and crucible; (**b**) EDS layered image of slag foam, layer between slag foam and wall of crucible and crucible.

EDS mapping of the spatial distribution of the elements of the slag foam, the layer between the slag foam and the wall of the crucible, and the crucible detected Al, O, Ca, Si, Mg, and Fe, as shown in Figure 9.

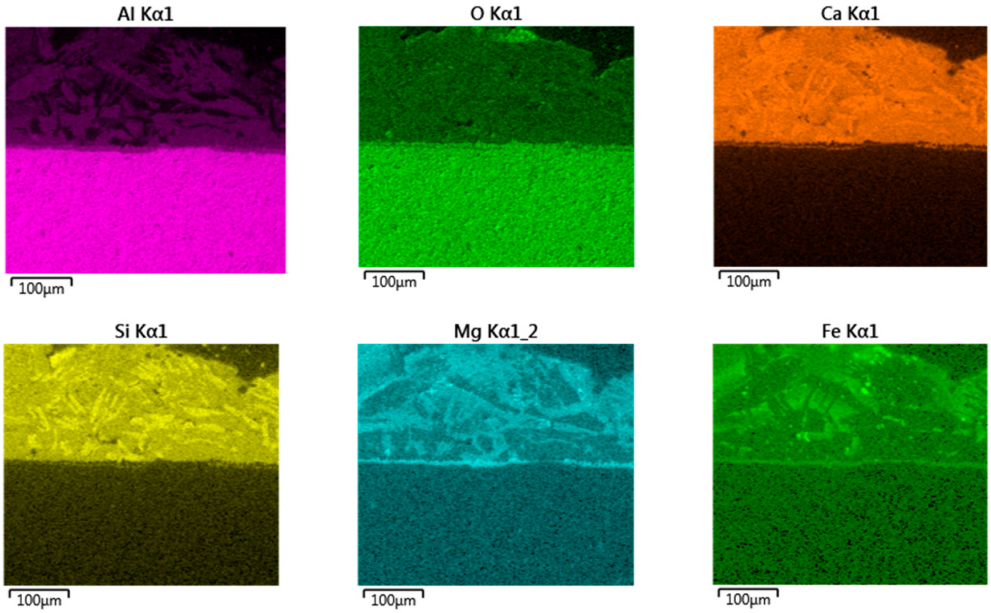

Figure 9. Energy-dispersive spectroscopy (EDS) mapping from scanning electron microscopy of elements of slag foam, layer between slag foam, and wall of crucible and crucible.

XRD analysis (Figure 10) of the slag foam and the layer between the slag foam and the wall of crucible identified the presence of the following phases: gehlenite, merwinite, corundum (Al_2O_3), and wuestite, as well as two spinels: magnesium aluminate ($MgAl_2O_4$) and magnesium iron oxide (Fe_2MgO_4). The presence of gehlenite, merwinite, and wuestite can be attributed to the slag foam, as XRD previously confirmed these phases (Figure 6a,b).

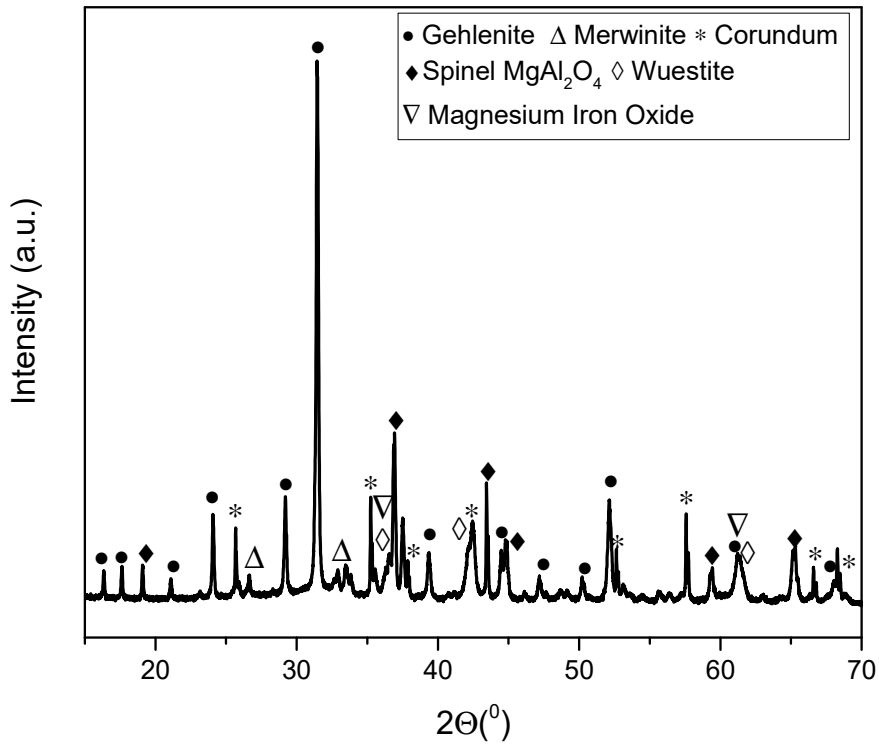

Figure 10. XRD analysis of slag foam, layer between slag foam and wall of crucible, and crucible.

The presence of peaks characterizing corundum is substantiated using alumina crucibles for this study. Based on the results of SEM/EDS, it can be assumed that the presence of phases such as gehlenite and two spinels refers to the layer between the slag foam and the crucible and can be explained by the activity of FeO and MgO, as well as by MgO and Al_2O_3 in liquid slag [50]. As reported in [19], slag with low basicity B3 and which has high amounts of FeO can be saturated by the spinel phases, including $MgAl_2O_4$ in its composition.

For all studied samples (Figure 11a–g), the Mossbauer spectra represent a doublet corresponding to the paramagnetic state of metallic iron Fe^{57} nuclei. The absence of sextuplet lines in the samples indicates that no magnetically ordered structures are formed with the participation of iron. The present paramagnetic component corresponds to iron nuclei in the valence state of Fe^{2+}.

Analysis of Mossbauer spectra revealed that two doublet lines in all cases approximate the paramagnetic component. The obtained values of the isomer shift (IS) and quadrupole splitting (QS) for the doublet components are in agreement with the parameters for crystalline wuestite FeO [51]. Both doublet components have close values of IS = 1.02 $\pm$ 0.05 mms^{-1} and different values of QS (Table 9).

The value of QS is determined by the symmetry of the close surroundings of the Fe^{57} nuclei and depends on the magnitude of the elastic deformation of the lattice; namely, the greater the deformation of the lattice, the higher the value of the QS. The presence of two doublet components with different quadrupole splitting values in the spectrum can be explained by the difference in the near environment of the Fe^{57} nuclei, which are in crystalline non-equivalent positions.

The non-equivalence of crystal positions of ferrous iron nuclei in the FeO structure can be related to the structural diversity of positions in the volume of the iron oxide particle and its surface layer. A higher QS value can reflect a more disordered nuclear environment of Fe^{57} than nuclei in the bulk of the particle, for which the near environment is more ordered [52].

In addition, the difference in the QS values of both components is possible due to different mechanisms of dense packing of anionic substructures, in particular, by packing octahedra ($Fe^{(II)}O_6$) connected to each other through faces or vertices [53]. These approaches correspond to the cubic and rhombohedral phases of FeO that were identified by XRD analysis (Figure 6a,b) and the presence of other reflexes, respectively, along with the main maxima for the rhombohedral phase [54].

Mossbauer spectroscopy allows for the detection of differences in Fe^{57} nuclei's positions for the cubic and rhombohedral phases by differentiating IS and QS of different doublet components. Therefore, the presence of both spectral doublets can be interpreted by different octahedron packings ($Fe^{(II)}O_6$) in the crystal structure of FeO of the studied slag foam samples.

Figure 12 shows the values of the quadrupole splitting of both doublets for each of the samples. A clear tendency of interdependence between the quadrupole splitting of both doublet components is observed: a decrease in the QS1 first doublet component of the sample is characterized by an increase in the QS2 second doublet component, respectively. Moreover, the value of QS1 represents a sequential order for all slag foam samples: Coke3 > Coke1:Bch > Anth > Bch > Coke2 > Coke1 > CPC. Similarly, the same consecutive order of values can be shown for QS2, which is increasing for slag foam samples: Coke3 < Coke1:Bch < Anth < Bch < Coke2 < Coke1 < CPC. Summarizing the dependence between QS1 and QS2, it can be concluded that the increase in the disorder of the environment of Fe^{57} nuclei in one of the non-equivalent positions leads to an ordering of the surroundings of the Fe^{57} nuclei in another position. Thus, there is a connection between the near-surface region and the particle volume: an increase in the ordering of the surface region corresponds to more ordering of the particle volume.

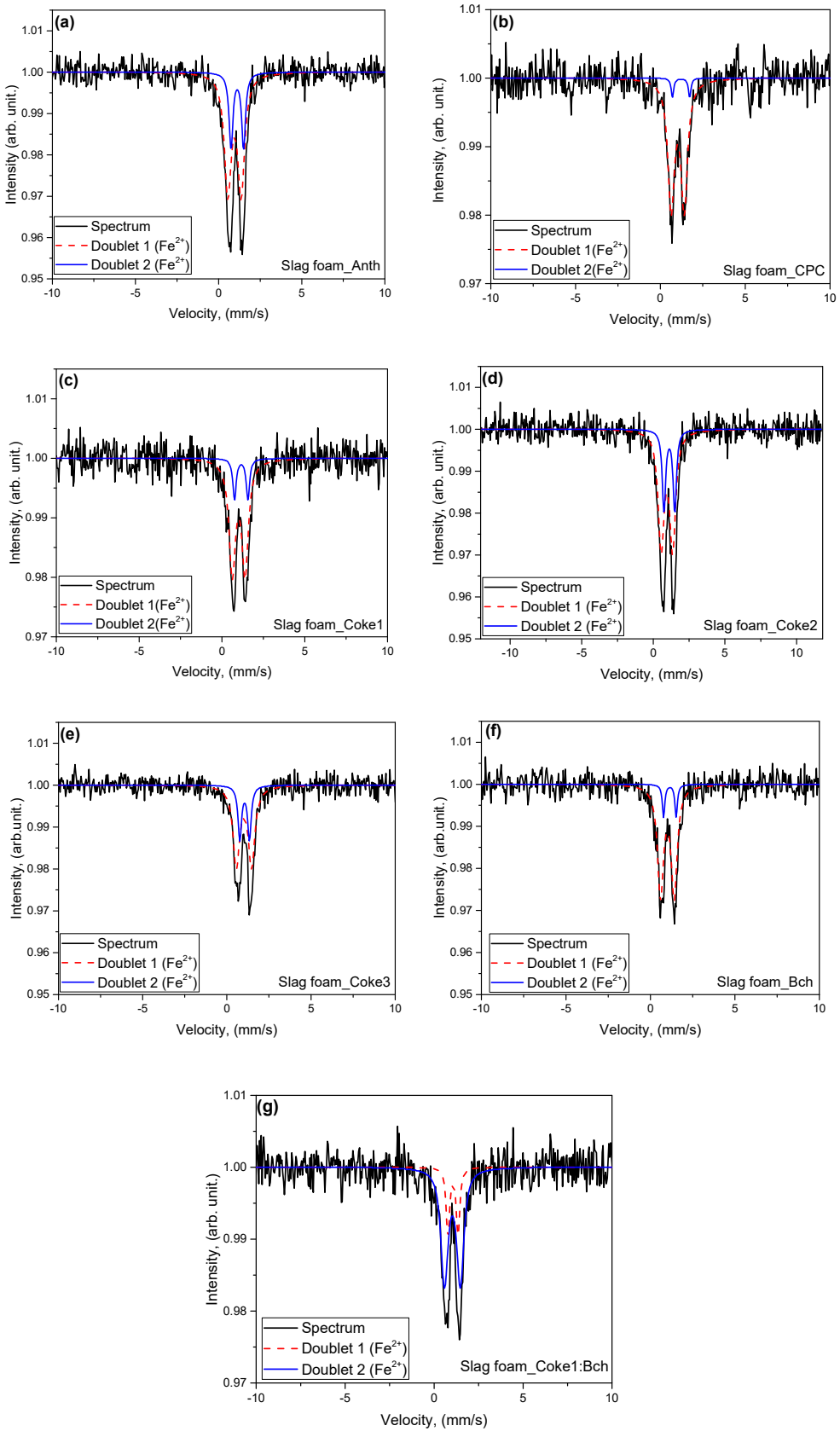

Figure 11. Mossbauer spectra of the slag foams using different carbon sources: (**a**) anthracite; (**b**) calcined petroleum coke (CPC); (**c**) coke1; (**d**) coke2; (**e**) coke3; and (**f**) biochar; and (**g**) 50 wt.% coke1:50 wt.% biochar.

Table 9. Mossbauer data on slag foam obtained using different carbon sources.

Sample	Component	IS, mm·s^{-1}	QS, mm·s^{-1}	H, Tesla	Relative intensity (%)	G, mm·s^{-1}	Interpretation
SF (Anth)	Doublet1 (Fe^{2+})	0.99	0.87	0	76	0.57	$Fe^{(II)}O_6$
	Doublet2 (Fe^{2+})	1.07	0.71	0	24	0.25	$Fe^{(II)}O_6$
SF (CPC)	Doublet1 (Fe^{2+})	1.02	0.77	0	94	0.46	$Fe^{(II)}O_6$
	Doublet2 (Fe^{2+})	1.22	1.02	0	6	0.17	$Fe^{(II)}O_6$
SF (Coke1)	Doublet1 (Fe^{2+})	1.01	0.77	0	84	0.47	$Fe^{(II)}O_6$
	Doublet2 (Fe^{2+})	1.17	0.81	0	16	0.24	$Fe^{(II)}O_6$
SF (Coke2)	Doublet1 (Fe^{2+})	0.95	0.80	0	71	0.49	$Fe^{(II)}O_6$
	Doublet2 (Fe^{2+})	1.12	0.76	0	29	0.29	$Fe^{(II)}O_6$
SF (Coke3)	Doublet1 (Fe^{2+})	1.02	0.91	0	74	0.46	$Fe^{(II)}O_6$
	Doublet2 (Fe^{2+})	1.06	0.57	0	26	0.25	$Fe^{(II)}O_6$
SF (Bch)	Doublet1 (Fe^{2+})	1.00	0.81	0	89	0.42	$Fe^{(II)}O_6$
	Doublet2 (Fe^{2+})	1.15	0.74	0	11	0.17	$Fe^{(II)}O_6$
SF (Coke1:Bch)	Doublet1 (Fe^{2+})	1.03	0.89	0	78	0.49	$Fe^{(II)}O_6$
	Doublet2 (Fe^{2+})	1.06	0.57	0	22	0.24	$Fe^{(II)}O_6$

IS, isomer shift relative to α-Fe; QS, quadrupole splitting; H, hyperfine magnetic field; G, ground state.

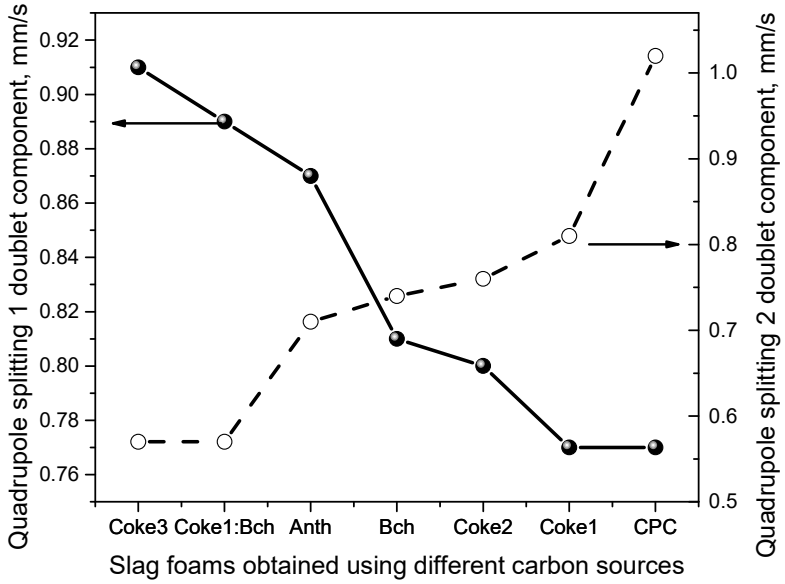

Figure 12. Quadrupole splitting of both doublets for each of the slag foam samples.

Figure 13 shows the contribution of the intensities of each doublet component to the total integrated intensity of the Mossbauer spectra of the samples.

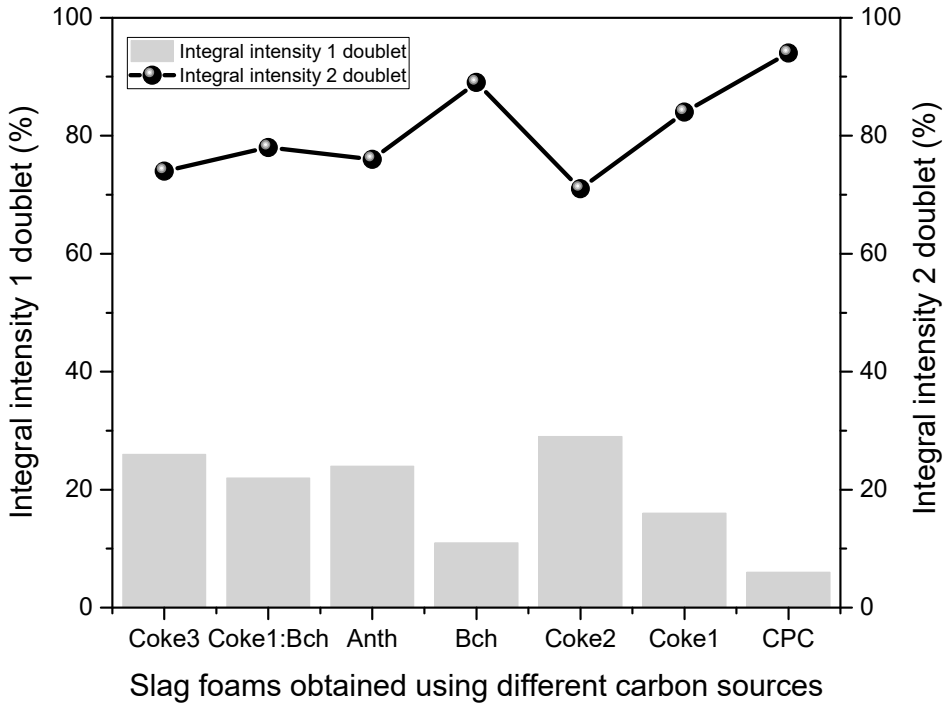

Figure 13. Integral intensity of each of the doublet components of the slag foam samples.

For all samples, the integrated intensity of the first doublet line is dominant and varies in the range of 72–94%. For this component, a higher value is observed in most samples of QS1, reflecting a more significant disorder in the environment around these Fe^{57} nuclei. Considering that the contribution of the doublet line intensity is proportional to the number of Fe^{57} nuclei and resonance absorption γ-quanta on which it is formed, it can be interpreted that exactly the first doublet line corresponds to iron nuclei located in the near-surface region of iron oxide particles. Moreover, they are characterized by rhombohedral packaging of packages ($Fe^{(II)}O_6$) with the possibility of including defects in the form of vacancies or implementation atoms. The second doublet line corresponds to Fe^{57} nuclei in the volume of iron oxide particles with cubic packing. Exceptions are slag foam (Coke1 and CPC) samples that are characterized by a more considerable QS value for the second doublet line.

Moreover, the contribution of the intensity of the second doublet line to the total integrated intensity is small for both samples and does not exceed 16%. The reason for this can be related to the low content of the wuestite phase and the small number of oxygen positions in these samples (Table 10). In this case, due to a lack of oxygen, the non-equivalent positions of the iron nuclei are not clearly expressed in the sense of forming a clear boundary near the surface area/volume of the particle. The formation of an oxide material that is homogeneous in terms of iron positions takes place, which includes regions with a more defective (disordered) environment, where there are inclusion regions with a more asymmetric defective environment of iron nuclei and, accordingly, a higher QS value.

Values of IS isomeric shifts of the doublet components of the Mossbauer spectra analyzed relative to the metallic α-Fe determine the chemical environment of Fe^{57} nuclei and their valence state. As mentioned, this made detecting the presence of Fe^{2+} ions and formation possible due to the synthesis of FeO oxide phases. The presence of two doublet lines with averaged values of isomeric shifts IS1 = 1.02 ± 0.05 mms^{-1} and IS2 = 1.11 ± 0.11 mms^{-1} indicates a partially different, although insignificant, chemical environment of the Fe^{57} nuclei, which arises as a result of their different surroundings

in the volume of particles and their surface region. The dynamics of the change in the isomeric shift for each sample (Figure 14) indicate that for the case of the first doublet component, a relatively constant value of IS1 is observed, which, according to the interpretation, corresponds to Fe^{57} iron nuclei in the volume of iron oxide particles.

Table 10. SEM/EDS analysis results of chemical composition for slag foam obtained using different carbon sources, wt.%.

Sample	O	Mg	Al	Si	Ca	Fe
SF (Anth)	35.98	4.11	11.67	8.70	21.85	17.70
SF (CPC)	36.30	4.42	8.37	10.57	23.76	16.58
SF (Coke1)	38.80	4.76	10.94	10.71	23.57	11.22
SF (Coke2)	38.63	3.82	8.79	10.32	23.06	15.39
SF (Coke3)	37.38	4.54	9.73	10.10	23.96	14.29
SF (Bch)	37.21	3.17	10.26	9.93	24.12	15.31
SF (Coke1:Bch)	38.18	4.63	9.48	10.77	25.52	11.42

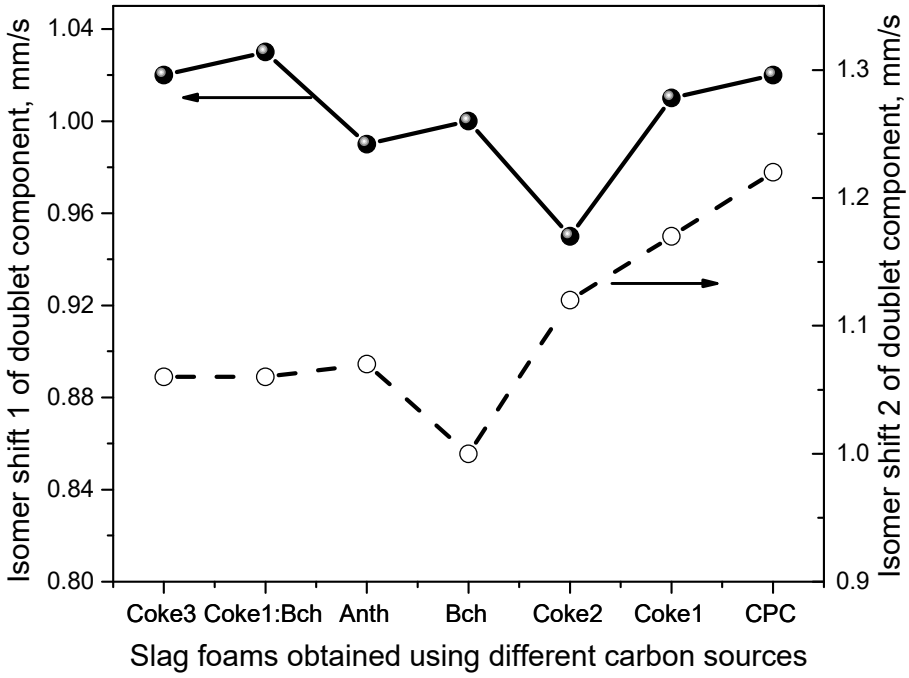

Figure 14. Magnitudes of isomeric shifts of doublet components of Mossbauer spectra.

The value of the isomeric shifts of the second doublet component IS2 for the samples forms a series of values that increase linearly for slag foam samples: Coke3 $\leq$ Coke1:Bch < Anth < Coke2 < Coke1 < CPC. The same trend was observed for the QS2 quadrupole moments, associated with increased disordering at the surface regions of iron oxide particles. Considering the values of the isomeric shifts, it can be assumed that an increase in disorder in the environment of Fe^{57} surface nuclei is associated with a growth in defectiveness of the structure. This causes a change in the chemical environment, particularly a possible change or delocalization of electrons, which in turn causes a difference in the covalence of chemical bonds. The exception is the sample SF (Bch), for which a lower value of the isomer shift IS2 = 1.00 mms^{-1} was noted. For this sample, the maximum value of the integrated intensity of the second component of the Mossbauer spectrum (89%) was observed, corresponding to the defective surface area of iron oxide particles.

Table 10 depicts the SEM/EDS analysis results of the chemical composition of slag foams. The elements Mg, Al, Si, Ca, and Fe were detected, previously determined by chemical analysis.

The investigated slag foam samples were characterized by scanning electron microscopy (SEM) and energy-dispersive spectroscopy (EDS) mapping from scanning electron microscopy of elements. The study by EDS mapping of the spatial distribution of the elements Ca, C, Al, O, Si, Fe, and Mg (Figures 15–21) clearly establishes correlations between elements, which provides information on the minerals that comprise the slag foams and confirmed the presence of all the elements identified by XRD (Figure 6a,b) and chemical analysis (Tables 6 and 7).

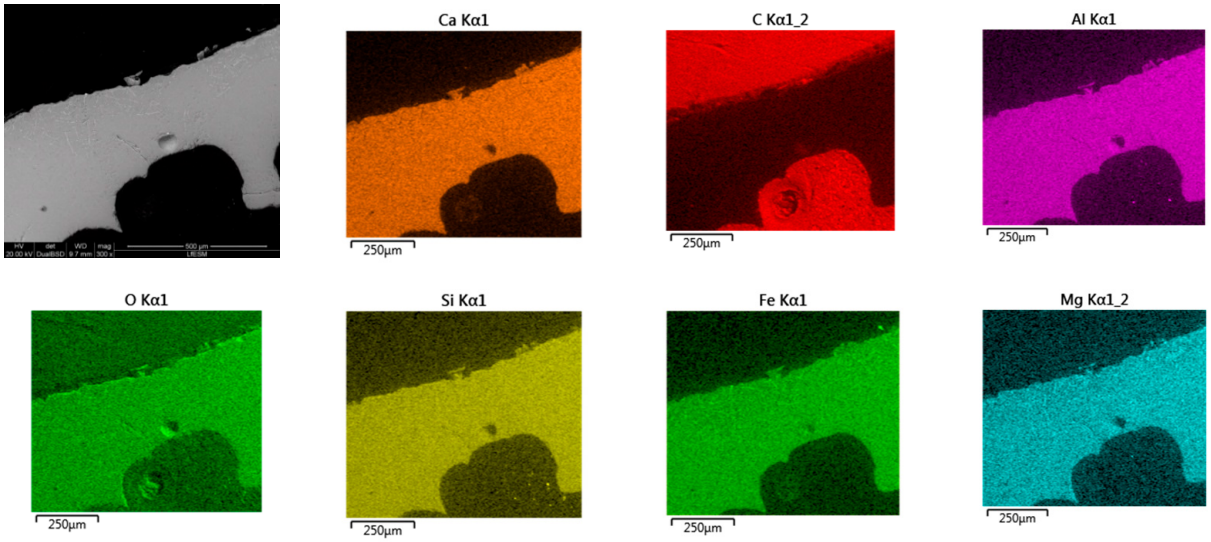

Figure 15. Energy-dispersive spectroscopy (EDS) mapping from scanning electron microscopy of elements in slag foam obtained using anthracite (Anth).

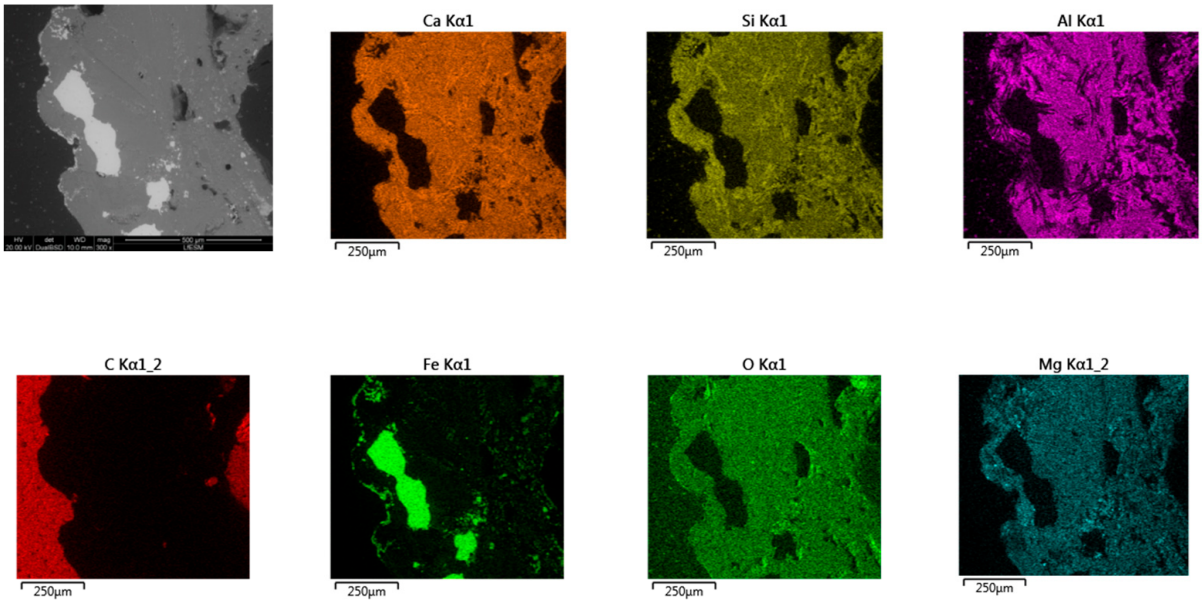

Figure 16. Energy-dispersive spectroscopy (EDS) mapping from scanning electron microscopy of elements in slag foam obtained using calcined petroleum coke (CPC).

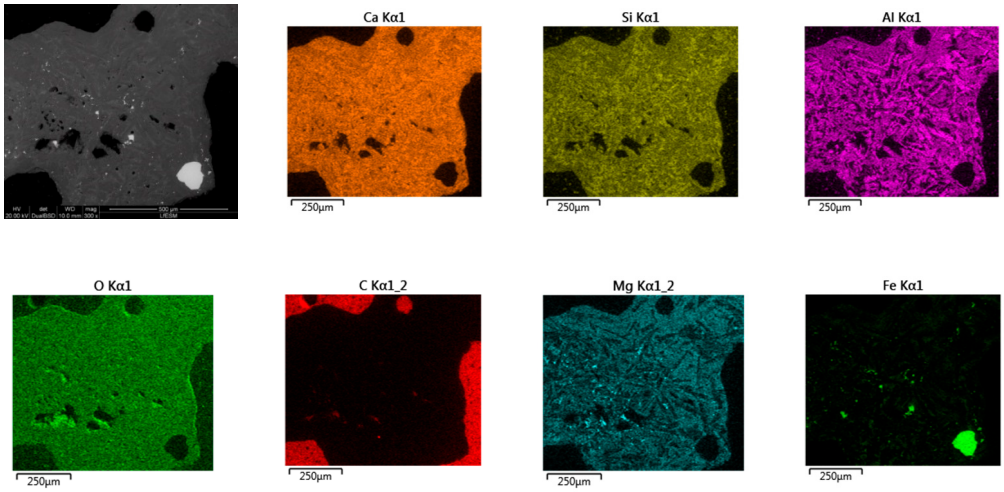

Figure 17. Energy-dispersive spectroscopy (EDS) mapping from scanning electron microscopy of elements in slag foam obtained using coke1.

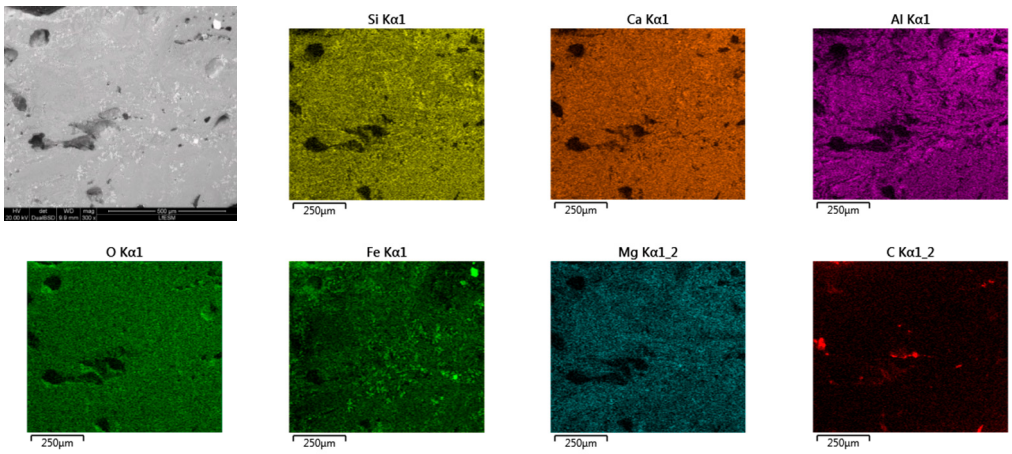

Figure 18. Energy-dispersive spectroscopy (EDS) mapping from scanning electron microscopy of elements in slag foam obtained using coke2.

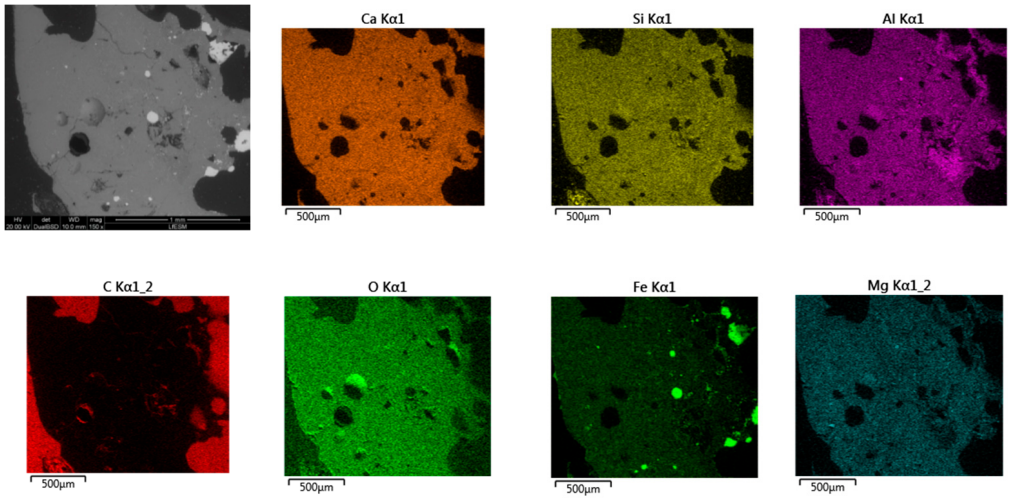

Figure 19. Energy-dispersive spectroscopy (EDS) mapping from scanning electron microscopy of elements in slag foam obtained using coke3.

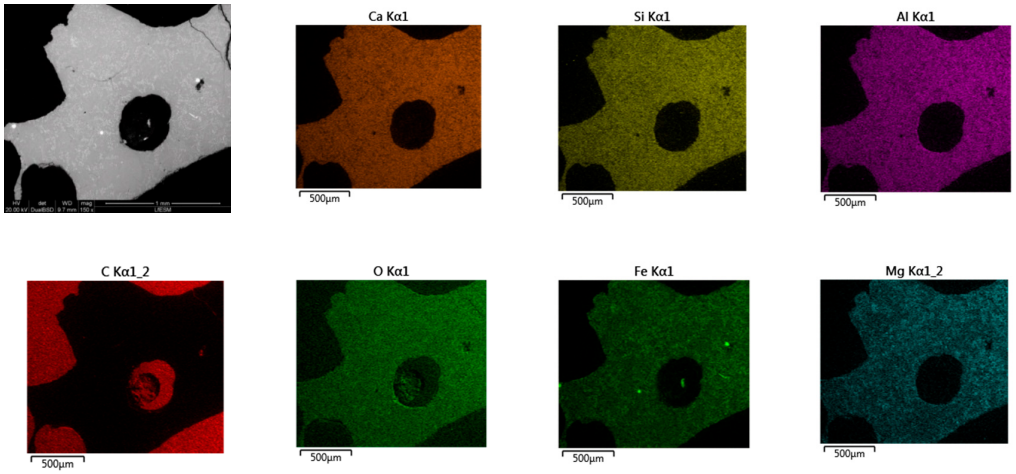

Figure 20. Energy-dispersive spectroscopy (EDS) mapping from scanning electron microscopy of elements in slag foam obtained using biochar (Bch).

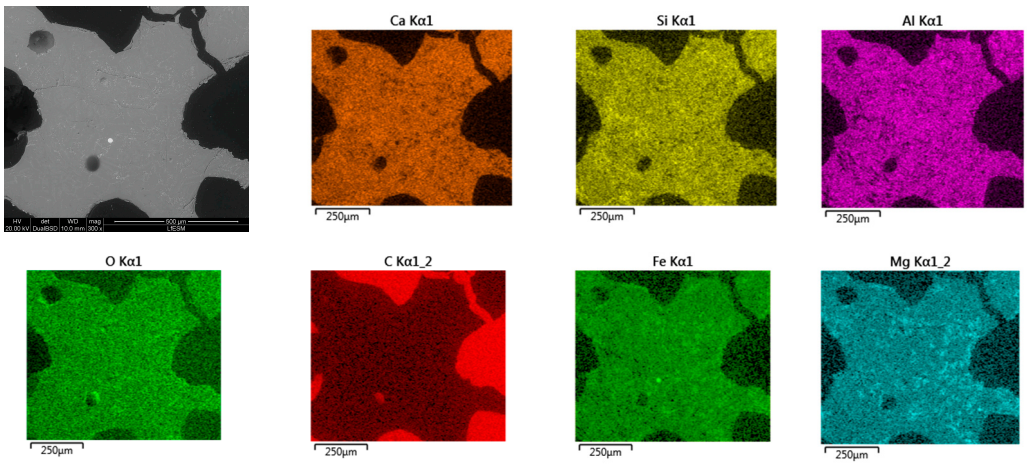

Figure 21. Energy-dispersive spectroscopy (EDS) mapping from scanning electron microscopy of elements in slag foam obtained using 50 wt.% coke:50 wt.% biochar.

The results of the slag foams' analysis by SEM/EDS analysis and EDS mapping in general show no adverse effect detectable on the chemical content of the slag foams when using biochar fully or partially.

4. Conclusions

The effect of six carbon sources on the foaming process was studied, of which three were conventional carbon-bearing sources: anthracite, calcined petroleum coke, and three samples of high-temperature cokes; and two were non-conventional carbon-bearing sources: biochar and a mixture of 50 wt.% biochar and 50 wt.% coke. Based on the results, the following conclusions can be drawn:

- Biochar showed the most inferior foaming characteristics due to the following. The low wettability of biochar by liquid slag prevents the reaction of carbon with FeO. The high reactivity of the biochar meant that FeO did not have time to react completely, and a smaller amount of CO was released, as evidenced by the value of the gas fraction (0.85). The low density meant that when adding biochar particles, they covered only the surface of slag foam and burned out on the slag foam surface very fast.
- Using the mixture of 50 wt.% coke and 50 wt.% biochar, the slag foaming process was improved and showed slag foaming characteristics similar to results obtained using conventional carbon sources. Based on the results obtained, it can be concluded that

biochar as a single carbon source cannot be recommended for use in slag foaming; however, when mixed with a conventional source, namely, coke, it showed promising results in EAF practice. Utilizing a biochar and coke1 mixture led to enhanced foaming compared to using biochar as the individual carbon source. Additionally, the observed foaming results obtained from the biochar and coke1 mixture were at a similar level as those achieved using other coke samples.

- A relationship was noticed between the XRD structural parameter crystallite height (L_c) of carbon sources and slag foaming characteristics (height and volume of slag foam). An increase in the structural ordering of the carbon material contributed to obtaining better slag foaming.
- The chemical composition of all slag foam samples showed no significant influence from the type of carbon source used. The decrease in the amount of Fe^{2+} after the foaming of the slag indicates a reduction reaction. The difference is between the top and bottom of the slag foam, as revealed by XRD. A maghemite (Fe_2O_3) and magnetite ($Mg_{0.4}Fe_{2.96}O_4$) crystalline phase in the top part of the slag foams is explained by the higher-valence iron oxide, probably located in the slag foam region in contact with air. At the same time, metallic iron was found at the bottom of all samples. A difference in the slag foam (mixture of coke and biochar) was found in the presence of such crystalline phases as magnesium iron oxide (Fe_2MgO_4) and magnetite ($Mg_{0.4}Fe_{2.96}O_4$).
- Based on SEM/EDS, it was noticed in many samples that there was a layer between the slag foam and the crucible wall, irrespective of the type of carbon source used. XRD analysis identified the following phases: gehlenite, merwinite, corundum (Al_2O_3), and wuestite, as well as two spinels: magnesium aluminate ($MgAl_2O_4$) and magnesium iron oxide (Fe_2MgO_4). It was assumed that the gehlenite and the two spinels could be attributed to the composition of the layer based on SEM/EDS.
- Mossbauer spectroscopy made it possible to obtain values of the isomer shift (IS) and quadrupole splitting (QS) for the doublet components that are in agreement with the parameters for crystalline wuestite (FeO). Through the analysis of interatomic magnetic interactions and the non-equivalent environment surrounding the nuclei, it was found that an increase in the disordering of nuclei in surface positions leads to a higher degree of order within the core of the particles. Additionally, a change in the chemical environment of the iron nuclei was observed, which was attributed to the defects present in the surface regions.

The findings of this study provide insight into the different impacts of various carbon sources, both conventional and non-conventional, on the foaming process. A noteworthy practical implication derived from the results is the viability of incorporating 50 wt.% biochar, a renewable carbon source, in combination with conventional carbon sources such as coke.

Author Contributions: Conceptualization, L.K. and J.S.; Investigation, L.K., A.K., A.H., H.H. and H.Z.; Methodology, L.K.; Supervision, J.S.; Writing—original draft, L.K.; Writing—review and editing, J.S., A.K., A.H. and H.H. All authors have read and agreed to the published version of the manuscript.

Funding: This research received no external funding.

Data Availability Statement: Not applicable.

Acknowledgments: Support by the scholarship program "Scholarship of the Scholarship Foundation of the Republic of Austria, Postdocs," (MPC-2022-02241), financed by the Federal Ministry of Education, Science, and Research of Austria, is gratefully acknowledged. Stahl- und Walzwerk Marienhütte GmbH, Graz, Austria, and voestalpine Stahl GmbH, Linz, Austria are also gratefully acknowledged for providing samples for research. The authors are also grateful to the reviewers for their insightful comments and efforts in improving the manuscript's text.

Conflicts of Interest: The authors declare no conflict of interest.

References

1. Agnihotri, A.; Singh, P.K.; Singh, D.; Gupta, M. Foamy Slag Practice to Enhance the Energy Efficiency of Electric Arc Furnace: An Industrial Scale Validation. *Mater. Today Proc.* **2021**, *46*, 1537–1542. [CrossRef]
2. Morales, R.D.; Rubén, L.G.; López, F.; Camacho, J.; Romero, J.A. The Slag Foaming Practice in EAF and Its Influence on the Steelmaking Shop Productivity. *ISIJ Int.* **1995**, *35*, 1054–1062. [CrossRef]
3. Matsuura, H.; Fruehan, R.J. Slag Foaming in an Electric Arc Furnace. *ISIJ Int.* **2009**, *49*, 1530–1535. [CrossRef]
4. Vieira, D.; de Almeida, R.A.M.; Bielefeldt, W.V.; Vilela, A.C.F. Slag Evaluation to Reduce Energy Consumption and EAF Electrical Instability. *Mat. Res.* **2016**, *19*, 1127–1131. [CrossRef]
5. Molloseau, C.L.; Fruehan, R.J. The Reaction Behavior of Fe-C-S Droplets in CaO-SiO_2-MgO-FeO Slags. *Met. Mater. Trans B* **2002**, *33*, 335–344. [CrossRef]
6. Kitamura, S.; Okohira, K. Influence of Slag Composition and Temperature on Slag Foaming. *ISIJ Int.* **1992**, *32*, 741–746. [CrossRef]
7. Zhu, T.X.; King, M.P.; Coley, K.S.; Irons, G.A. Erratum to: Progress in Slag Foaming in Metallurgical Processes. *Met. Mater. Trans. B* **2013**, *44*, 478. [CrossRef]
8. Vidacak, B.; Arvanitidis, I.; Jönsson, P.G.; Sjöberg, P. Observation on Foaming of EAF Slags in the Production of Stainless Steel: Observation on Foaming of EAF Slags. *Scand. J. Metall.* **2002**, *31*, 321–327. [CrossRef]
9. Jung, S.-M.; Fruehan, R.J. Foaming Characteristics of BOF Slags. *ISIJ Int.* **2000**, *40*, 348–355. [CrossRef]
10. Wang, R.; Zhang, B.; Liang, Y.; Liu, C.; Jiang, M. Micro Insight into Foaming Behavior of CaO–SiO_2–FeO–MgO-Based Slag Induced by Slag/Metal Reaction. *Ceram. Int.* **2023**, *49*, 17185–17193. [CrossRef]
11. Wang, R.; Zhang, B.; Hu, C.; Liu, C.; Jiang, M. Study on Splashing Mechanism in Basic Oxygen Furnace Based on Slag Foaming Modeling. *Steel Res. Int.* **2022**, *93*, 2100318. [CrossRef]
12. Zhang, Y.; Fruehan, R.J. Effect of the Bubble Size and Chemical Reactions on Slag Foaming. *MMTB* **1995**, *26*, 803–812. [CrossRef]
13. European Commission. *Directorate General for Research and Innovation. Sustainable EAF Steel Production (GREENEAF)*; Publications Office: Luxembourg, 2013.
14. Luz, A.P.; Tomba Martinez, A.G.; López, F.; Bonadia, P.; Pandolfelli, V.C. Slag Foaming Practice in the Steelmaking Process. *Ceram. Int.* **2018**, *44*, 8727–8741. [CrossRef]
15. Chychko, A.; Seetharaman, S. Foaming in Electric Arc Furnace Part I: Laboratory Studies of Enthalpy Changes of Carbonate Additions to Slag Melts. *Met. Mater. Trans. B* **2011**, *42*, 20–29. [CrossRef]
16. Kim, H.S.; Min, D.J.; Park, J.H. Foaming Behavior of CaO-SiO_2-FeO-MgOsatd-X (X=Al_2O_3,MnO, P_2O_5, and CaF_2) Slags at High Temperatures. *ISIJ Int.* **2001**, *41*, 317–324. [CrossRef]
17. Leonard, D.C.; Bonte, L.; Dufour, A.; Ferstl, A.; Raipala, K.; Scmole, P.; Schoone, P.; Verduras, J.L.; Willmers, R.R. Coke Quality Requirements of European Blast Furnace Engineers. In Proceedings of the Proceedings 3rd European Cokemaking Congress, Gent, Belgium, 16–18 September 1996.
18. Bhoi, B.; Jouhari, A.K.; Ray, H.S.; Misra, V.N. Smelting Reduction Reactions by Solid Carbon Using Induction Furnace: Foaming Behaviour and Kinetics of FeO Reduction in CaO–SiO_2–FeO Slag. *Ironmak. Steelmak.* **2006**, *33*, 245–252. [CrossRef]
19. Luz, A.P.; Avila, T.A.; Bonadia, P.; Pandolfelli, V.C. Slag Foaming: Fundamentals, Experimental Evaluation and Application in the Steelmaking Industry. *Refract. Worldforum* **2011**, *3*, 91–98.
20. Zhang, Y.; Fruehan, R.J. Effect of Carbonaceous Particles on Slag Foaming. *MMTB* **1995**, *26*, 813–819. [CrossRef]
21. Ogawa, Y.; Katayama, H.; Hirata, H.; Tokumitsu, N.; Yamauchi, M. Slag Foaming in Smelting Reduction and Its Control with Carbonaceous Materials. *ISIJ Int.* **1992**, *32*, 87–94. [CrossRef]
22. Wu, K.; Qian, W.; Chu, S.; Niu, Q.; Luo, H. Behavior of Slag Foaming Caused by Blowing Gas in Molten Slags. *ISIJ Int.* **2000**, *40*, 954–957. [CrossRef]
23. Corbari, R.; Matsuura, H.; Halder, S.; Walker, M.; Fruehan, R.J. Foaming and the Rate of the Carbon-Iron Oxide Reaction in Slag. *Met. Mater. Trans. B* **2009**, *40*, 940–948. [CrossRef]
24. Ji, F.-Z.; Barati, M.; Coley, K.; Irons, G.A. Kinetics of coal injection into iron oxide containing slags. *Can. Metall. Q.* **2005**, *44*, 85–94. [CrossRef]
25. Kieush, L.; Rieger, J.; Schenk, J.; Brondi, C.; Rovelli, D.; Echterhof, T.; Cirilli, F.; Thaler, C.; Jaeger, N.; Snaet, D.; et al. A Comprehensive Review of Secondary Carbon Bio-Carriers for Application in Metallurgical Processes: Utilization of Torrefied Biomass in Steel Production. *Metals* **2022**, *12*, 2005. [CrossRef]
26. Kieush, L.; Schenk, J.; Koveria, A.; Rantitsch, G.; Hrubiak, A.; Hopfinger, H. Utilization of Renewable Carbon in Electric Arc Furnace-Based Steel Production: Comparative Evaluation of Properties of Conventional and Non-Conventional Carbon-Bearing Sources. *Metals* **2023**, *13*, 722. [CrossRef]
27. DiGiovanni, C.; Li, D.; Ng, K.W.; Huang, X. Ranking of Injection Biochar for Slag Foaming Applications in Steelmaking. *Metals* **2023**, *13*, 1003. [CrossRef]
28. Ismail, A.N.; Yunos, N.F.D.M.; Rajeswari, M.S.R.; Idris, M.A. Production of Metallic Iron from Electric Arc Furnace (EAF) Slag Using Palm Shells Char/Coke Blends. In Proceedings of the AIP Conference Proceedings, Arau, Malaysia, 3 May 2021; p. 020202.
29. Sahajwalla, V. Recycling Waste Plastics in EAF Steelmaking: Carbon/Slag Interactions of HDPE-Coke Blends. *Steel Res. Int.* **2009**, *80*, 535–543. [CrossRef]
30. Kongkarat, S.; Khanna, R.; Koshy, P.; O'kane, P.; Sahajwalla, V. Recycling Waste Polymers in EAF Steelmaking: Influence of Polymer Composition on Carbon/Slag Interactions. *ISIJ Int.* **2012**, *52*, 385–393. [CrossRef]

31. Zaharia, M.; Sahajwalla, V.; Kim, B.-C.; Khanna, R.; Saha-Chaudhury, N.; O'Kane, P.; Dicker, J.; Skidmore, C.; Knights, D. Recycling of Rubber Tires in Electric Arc Furnace Steelmaking: Simultaneous Combustion of Metallurgical Coke and Rubber Tyres Blends. *Energy Fuels* **2009**, *23*, 2467–2474. [CrossRef]
32. Maroufi, S.; Mayyas, M.; Mansuri, I.; O'Kane, P.; Skidmore, C.; Jin, Z.; Fontana, A.; Sahajwalla, V. Study of Reaction Between Slag and Carbonaceous Materials. *Met. Mater. Trans. B* **2017**, *48*, 2316–2323. [CrossRef]
33. Yunos, N.F.M.; Zaharia, M.; Idris, M.A.; Nath, D.; Khanna, R.; Sahajwalla, V. Recycling Agricultural Waste from Palm Shells during Electric Arc Furnace Steelmaking. *Energy Fuels* **2012**, *26*, 278–286. [CrossRef]
34. Fidalgo, B.; Berrueco, C.; Millan, M. Chars from Agricultural Wastes as Greener Fuels for Electric Arc Furnaces. *J. Anal. Appl. Pyrolysis* **2015**, *113*, 274–280. [CrossRef]
35. Huang, X.-A.; Ng, K.W.; Giroux, L.; Duchesne, M. Carbonaceous Material Properties and Their Interactions with Slag During Electric Arc Furnace Steelmaking. *Met. Mater. Trans. B* **2019**, *50*, 1387–1398. [CrossRef]
36. Echterhof, T. Review on the Use of Alternative Carbon Sources in EAF Steelmaking. *Metals* **2021**, *11*, 222. [CrossRef]
37. Heo, J.H.; Park, J.H. Assessment of Physicochemical Properties of Electrical Arc Furnace Slag and Their Effects on Foamability. *Met. Mater Trans. B* **2019**, *50*, 2959–2968. [CrossRef]
38. Stadler, S.A.C.; Eksteen, J.J.; Aldrich, C. Physical Modelling of Slag Foaming in Two-Phase and Three-Phase Systems in the Churn-Flow Regime. *Miner. Eng.* **2006**, *19*, 237–245. [CrossRef]
39. Matsuura, H.; Manning, C.P.; Fortes, R.A.F.O.; Fruehan, R.J. Development of a Decarburization and Slag Formation Model for the Electric Arc Furnace. *ISIJ Int.* **2008**, *48*, 1197–1205. [CrossRef]
40. Fruehan, R.J.; Goldstein, D.; Sarma, B.; Story, S.R.; Glaws, P.C.; Pasewicz, H.U. Recent Advances in the Fundamentals of the Kinetics of Steelmaking Reactions. *Met. Mater Trans. B* **2000**, *31*, 891–898. [CrossRef]
41. Hong, L.; Hirasawa, M.; Sano, M. Behavior of Slag Foaming with Reduction of Iron Oxide in Molten Slags by Graphite. *ISIJ Int.* **1998**, *38*, 1339–1345. [CrossRef]
42. Xiang, J.; Wang, X.; Yang, M.; Wang, J.; Shan, C.; Fan, G.; Qiu, G.; Lv, X. Slag-Foaming Phenomenon Originating from Reaction of Titanium-Bearing Blast Furnace Slag: Continuous Monitoring of Foaming Height and Calibration. *J. Mater. Res. Technol.* **2021**, *11*, 1184–1192. [CrossRef]
43. Kieush, L.; Schenk, J.; Pfeiffer, A.; Koveria, A.; Rantitsch, G.; Hopfinger, H. Investigation on the Influence of Wood Pellets on the Reactivity of Coke with CO_2 and Its Microstructure Properties. *Fuel* **2022**, *309*, 122151. [CrossRef]
44. Bazaluk, O.; Kieush, L.; Koveria, A.; Schenk, J.; Pfeiffer, A.; Zheng, H.; Lozynskyi, V. Metallurgical Coke Production with Biomass Additives: Study of Biocoke Properties for Blast Furnace and Submerged Arc Furnace Purposes. *Materials* **2022**, *15*, 1147. [CrossRef]
45. Kieush, L.; Boyko, M.; Koveria, A.; Yaholnyk, M.; Poliakova, N. Manganese Sinter Production with Wood Biomass Application. *KEM* **2020**, *844*, 124–134. [CrossRef]
46. Sahajwalla, V.; Zaharia, M.; Kongkarat, S.; Khanna, R.; Rahman, M.; Saha-Chaudhury, N.; O'Kane, P.; Dicker, J.; Skidmore, C.; Knights, D. Recycling End-of-Life Polymers in an Electric Arc Furnace Steelmaking Process: Fundamentals of Polymer Reactions with Slag and Metal. *Energy Fuels* **2012**, *26*, 58–66. [CrossRef]
47. Almeida, R.A.M.D.; Vieira, D.; Bielefeldt, W.V.; Vilela, A.C.F. MgO Saturation Analisys of CaO-SiO_2-FeO-MgO-Al_2O_3 Slag System. *Mat. Res.* **2017**, *21*, 1–8. [CrossRef]
48. Luz, A.P.; Vivaldini, D.O.; López, F.; Brant, P.O.R.C.; Pandolfelli, V.C. Recycling MgO–C Refractories and Dolomite Fines as Slag Foaming Conditioners: Experimental and Thermodynamic Evaluations. *Ceram. Int.* **2013**, *39*, 8079–8085. [CrossRef]
49. Chang, Y.-E.; Lin, C.-M.; Shen, J.-M.; Chang, W.-T.; Wu, W. Effect of MgO Content on the Viscosity, Foaming Life, and Bonding in Liquid and Liquid/Solid CaO-SiO_2-MgO-5Al_2O_3-30FeO Slags. *Metals* **2021**, *11*, 249. [CrossRef]
50. Pretorius, E.; Carlisle, R.C. Foamy Slag Fundamentals and Their Practical Application to Electric Furnace Steelmaking. *Iron Steelmak.* **1999**, *26*, 79–88.
51. Aldon, L.; Jumas, J.-C. Lithium-Induced Conversion Reaction in Wüstite $Fe_{1-x}O$ Studied by 57Fe Mössbauer Spectroscopy. *Solid State Sci.* **2012**, *14*, 354–361. [CrossRef]
52. Bazaluk, O.; Hrubiak, A.; Moklyak, V.; Moklyak, M.; Kieush, L.; Rachiy, B.; Gasyuk, I.; Yavorskyi, Y.; Koveria, A.; Lozynskyi, V.; et al. Structurally Dependent Electrochemical Properties of Ultrafine Superparamagnetic 'Core/Shell' γ-Fe_2O_3/Defective α-Fe_2O_3 Composites in Hybrid Supercapacitors. *Materials* **2021**, *14*, 6977. [CrossRef]
53. Cornell, R.M.; Schwertmann, U. *The Iron Oxides: Structure, Properties, Reactions, Occurences and Uses*, 1st ed.; Wiley: Hoboken, NJ, USA, 2003; ISBN 978-3-527-30274-1.
54. Ajinkya, N.; Yu, X.; Kaithal, P.; Luo, H.; Somani, P.; Ramakrishna, S. Magnetic Iron Oxide Nanoparticle (IONP) Synthesis to Applications: Present and Future. *Materials* **2020**, *13*, 4644. [CrossRef]